nature nanotechnology

ARTICLES

https://doi.org/10.1038/s41565-022-01115-2

Check for updates

Electric control of valley polarization in monolayer WSe_2 using a van der Waals magnet

Jia-Xin Li[1,7], Wei-Qing Li[1,7], Sheng-Hsiung Hung[2,7], Po-Liang Chen[1], Yueh-Chiang Yang[3], Tian-Yun Chang[1], Po-Wen Chiu[3,4], Horng-Tay Jeng[2,5,6] ✉ and Chang-Hua Liu[1,3] ✉

Electrical manipulation of the valley degree of freedom in transition metal dichalcogenides is central to developing valleytronics. Towards this end, ferromagnetic contacts, such as Ga(Mn)As and permalloy, have been exploited to inject spin-polarized carriers into transition metal dichalcogenides to realize valley-dependent polarization. However, these materials require either a high external magnetic field or complicated epitaxial growth steps, limiting their practical applications. Here we report van der Waals heterostructures based on a monolayer WSe_2 and an Fe_3GeTe_2/hexagonal boron nitride ferromagnetic tunnelling contact that under a bias voltage can effectively inject spin-polarized holes into WSe_2, leading to a population imbalance between ±K valleys, as confirmed by density functional theory calculations and helicity-dependent electroluminescence measurements. Under an external magnetic field, we observe that the helicity of electroluminescence flips its sign and exhibits a hysteresis loop in agreement with the magnetic hysteresis loop obtained from reflective magnetic circular dichroism characterizations on Fe_3GeTe_2. Our results could address key challenges of valleytronics and prove promising for van der Waals magnets for magneto-optoelectronics applications.

The monolayer semiconducting transition metal dichalcogenides (TMDs), which exhibit exotic excitonic and spin–valley properties, have attracted considerable attention in recent years[1–3]. They possess direct bandgaps located at energy-degenerate valleys (±K) in the hexagonal Brillouin zone. The electrons and holes can bind together within each valley at room temperature to form valley excitons, which are tightly bound due to quantum confinement, reduced screening effects and large electron and hole effective masses. Furthermore, the large spin–orbit coupling together with inversion symmetry breaking of monolayer TMDs cause the charge carriers in two inequivalent valleys to have opposite spins (that is, spin–valley locking) as well as exhibiting different optical selection rules[1–3]. By exploiting these spin–valley properties, it is possible to selectively polarize electrons, holes and excitons to the K or −K valley by illuminating the monolayer TMDs with σ^+-polarized or σ^--polarized light, respectively, as confirmed by photoluminescence (PL), valley Hall and exciton Hall measurements[4–8]. These initial investigations highlight the possibility of optically manipulating the valley degree of freedom of TMDs.

Towards practical device applications, continued efforts further demonstrate electrical control of the valley polarization by exploiting ferromagnetic materials. Pioneering work utilized the ferromagnetic semiconductor Ga(Mn)As to inject spin-polarized charge carriers into a specific valley and observed valley-polarized light emission[9]. However, such a device relies on sophisticated bottom-up material growth steps, limiting the structures and integrability of devices. Although the challenges can be overcome by using permalloy for local electrodes to inject spin-polarized carriers, such a structure requires high external magnetic fields to observe the valley-dependent light emission, probably due to the polycrystalline nature of permalloy[10].

In contrast, exploiting the emerging van der Waals (vdW) ferromagnetic metal Fe_3GeTe_2 (FGT) as a spin injector could potentially offer unprecedented opportunities. One essential reason is that FGT can be readily integrated with TMDs or other layered materials to form vdW heterostructures, which enable pristine interfaces without the issue of lattice mismatch[11–13]. Moreover, multiple previous works indicate that ultrathin FGT has a Curie temperature higher than 130 K and can exhibit a nearly square-shaped magnetic hysteresis loop with large coercivity, revealing that it possesses a single magnetic domain as well as strong perpendicular magnetic anisotropy[14,15]. By using ionic liquid gating, it is possible to further elevate the Curie temperature of ultrathin FGT to room temperature[16]. On the basis of these fundamental studies, multiple works have shown the great potential of using FGT as electrodes for spin-valve applications[17]. However, further application of FGT towards magneto-optoelectronics and valleytronics remains largely unexplored experimentally. Here, we demonstrate a novel vdW heterostructure that incorporates an ultrathin FGT-based ferromagnetic tunnel contact. By conducting helicity-resolved electroluminescence (EL) experiments and density functional theory calculations, we show that the FGT contact can inject spin-polarized holes into a monolayer WSe_2 and lead to valley polarization. Additionally, when sweeping the direction of the external magnetic field, the helicity of EL generated from WSe_2 not only flips its sign, but also shows a nearly square hysteresis loop. This agrees well with magnetic hysteresis loops derived from our reflective magnetic circular dichroism (RMCD) measurements of FGT. Our work provides a new route to electrically control the valley-dependent polarization of TMDs, a crucial step towards modern optoelectronics and information processing applications[18].

Sample design

Figure 1a,b shows a schematic and an optical image of the investigated vdW heterostructures. Detailed descriptions of the material preparation, characterization and fabrication of heterostructures

[1]Institute of Photonics Technologies, National Tsing Hua University, Hsinchu, Taiwan. [2]Department of Physics, National Tsing Hua University, Hsinchu, Taiwan. [3]Department of Electrical Engineering, National Tsing Hua University, Hsinchu, Taiwan. [4]Institute of Atomic and Molecular Sciences, Academia Sinica, Taipei, Taiwan. [5]Institute of Physics, Academia Sinica, Taipei, Taiwan. [6]Physics Division, National Center for Theoretical Sciences, Hsinchu, Taiwan. [7]These authors contributed equally: Jia-Xin Li, Wei-Qing Li, Sheng-Hsiung Hung. ✉e-mail: jeng@phys.nthu.edu.tw; chliu@ee.nthu.edu.tw

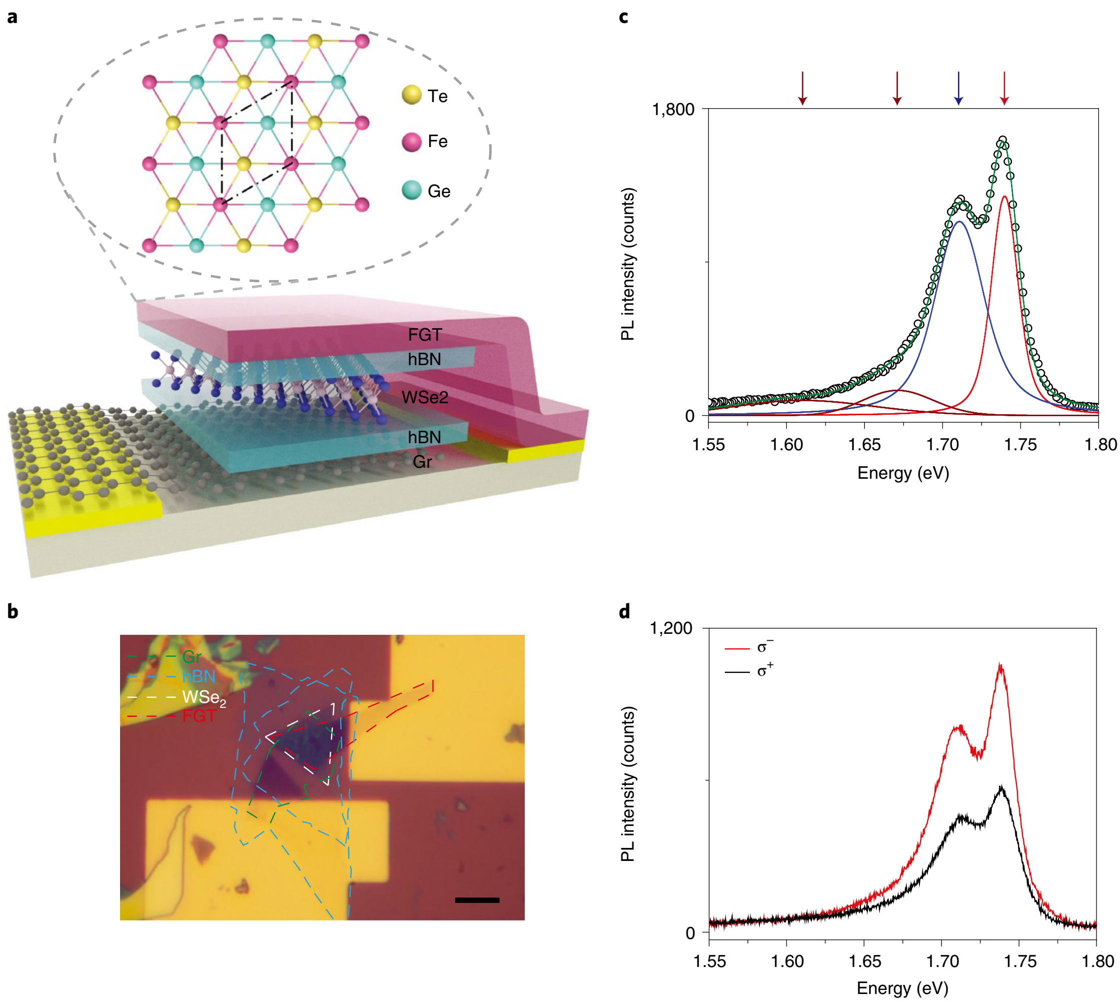

Fig. 1 | Device structure and optical generation of valley polarization. a, Schematic of the top view of the FGT crystal structure and the device configuration, composed of vertically stacked FGT/hBN/chemical vapour deposited (CVD) WSe_2/hBN/graphene (top to bottom) heterostructures. The unit cell of FGT is enclosed by the black dashed lines. Gr, graphene. **b**, Optical microscope image of the vdW heterostructures. Scale bar, 10 μm. **c**, PL spectrum (not polarization resolved) for 1.96 eV excitation. The spectrum was fitted by using Voigt functions to identify different excitonic peaks, where red, blue and brown solid lines refer to the spectra of neutral (X^0), charged ($X^{+/-}$) and impurity-bound (X^{L1} and X^{L2}) excitonic emissions, respectively, and the arrows indicate their peak energies. The green solid line is the cumulative fitting of all curves. The open black circles represent experimental data. **d**, Polarization-resolved PL spectra for σ^- and σ^+ detection. The incident laser is σ^- polarized.

are provided in Methods and Supplementary Section 1. The heterostructures are composed of monolayer WSe_2 sandwiched between the graphene/hexagonal boron nitride (hBN) bottom tunnelling contact and FGT/hBN top ferromagnetic tunnelling contact. WSe_2 and graphene act as the emissive layer and bottom electrode, respectively. The FGT is ~6.4 nm thick, and serves as the top electrode, which can inject spin-polarized carriers into ±K valleys in WSe_2. The insulating hBN layers behave as tunnel barriers, which prevent the problem of conductance mismatch between the FGT ferromagnetic metal and WSe_2 semiconductor. Moreover, for optimal device performances, we selected bilayer hBN flakes as the tunnelling barriers to ensure that carriers can effectively tunnel from two electrodes into WSe_2, without being trapped at surface states, and these injected carriers have long enough lifetime to form excitons[19–21].

PL and EL characterizations

We started by using PL spectroscopy to characterize the optical properties of the sandwiched WSe_2 in the out-of-plane direction. The measurement was conducted at a temperature of 78 K with an excitation energy of 1.96 eV and spot size ~1 μm. Figure 1c shows the PL spectrum, which is fitted well by using multiple peaks with Voigt lineshapes. The extracted peaks at ~1.74 eV and ~1.71 eV originate from the neutral exciton (X^0) and charged exciton ($X^{+/-}$) emissions, respectively. The other two Voigt lineshapes, which peak at lower energies (~1.67 eV and ~1.61 eV), are associated with the impurity-bound excitons, denoted as X^{L1} and X^{L2} respectively[22–24]. We note that these characteristic lineshapes are also observed in the following EL measurements of WSe_2. To probe their valley excitonic features, we conducted a circular-polarization-resolved PL measurement (Fig. 1d). The result shows that the emissions of X^0, $X^{+/-}$ and X^{L1} exhibit a stronger σ^- component, following the helicity of the incident laser, and their degrees of circular polarization are $\rho_{X^0} = 36.6\%$, $\rho_{X^{+/-}} = 26\%$ and $\rho_{X^{L1}} = 33\%$, respectively. These helicities are calculated using the equation $\rho = \frac{I_- - I_+}{I_- + I_+}$, where I_- and I_+ represent the extracted peak intensity of the σ^--polarized and σ^+-polarized component (see Supplementary Section 2 for the calculation of degrees of polarization and additional data taken under σ^+ laser excitation). The observed PL helicity clearly indicates that the valley degrees of freedom of the WSe_2 used can be selectively addressed.

Next, we examine the feasibility of generating EL from the WSe_2 layer. Figure 2a plots the current as a function of the bias voltage (V_b) applied across the graphene and FGT electrodes. The top FGT is connected to ground in this I–V_b measurement and all of the following optoelectronic experiments, unless otherwise specified. The curve exhibits rectifying behaviour under the positive and negative bias regions, indicating that charge carriers can tunnel through the atomically thin hBN barriers. These injected carriers then form excitons and radiatively recombine in the monolayer WSe_2, giving rise to EL as schematically illustrated in Fig. 2b,c. Figure 2d presents the colour map of the EL spectra (not polarization resolved) as a function of current injection (also see Supplementary Section 3 for an EL spatial map). The result clearly shows that the EL becomes observable at $|V_b|$ around 2 V and a current of 200 nA, and EL is enhanced as the current injection increases to 3 μA.

To gain further insight, we analysed the EL spectra as shown in Fig. 2e,f, operated at $V_b = -2.5$ V and $V_b = 2.4$ V respectively. The peaks of neutral, charged and impurity-bound excitons could be identified from the fits, but it is notable that these two EL spectra show distinct features. Under the negative V_b, the EL spectrum is dominant by the emissions of neutral and charged excitons, similar to the PL result shown in Fig. 1c. In contrast, under the positive V_b, the emissions of impurity-bound excitons play a dominant role. The observed EL with asymmetric spectral weight under positive and negative V_b can be attributed to the density of states of FGT, which exhibits different characters below and above its Fermi level (see Supplementary Section 4 for further discussion). In addition, we characterized the collection losses of the set-up of EL measurement and found that the extrinsic quantum efficiency of our device could reach 0.11% (Supplementary Section 5), comparable to those of the previously reported emitters, which were composed of a monolayer WSe_2 sandwiched between the graphene/hBN tunnelling contacts[19,20]. The result indicates that the ultrathin FGT is optically transparent, which cannot be realized by using conventional iron-group metals as local electrodes.

Evidence for electric control of valley polarization

Following this, we applied an external magnetic field (Faraday geometry) to the heterostructures and analysed the effect on EL helicity. Figure 3a shows the helicity-resolved EL spectra with $V_b = -2.5$ V and 0.5 T out-of-plane magnetic field. The measured EL spectra exhibit stronger σ^--polarized component for different excitonic transitions ($\rho_{X^0} = 8.6\%$, $\rho_{X^{+/-}} = 5.6\%$ and $\rho_{X^{L1}} = 9.2\%$; see Supplementary Section 6 for the fits and calculations). We find that the observed EL helicity is still preserved after switching off the external magnetic field (Supplementary Section 7), but the helicity flips sign when the field is directed in the opposite direction (Fig. 3b). Similar EL helicity switching behaviour can also be observed when operating the heterostructures at different negative bias voltages. However, this switching phenomenon vanishes if we operate the FGT-based heterostructures at room temperature (Supplementary Section 8) or replace the top ferromagnetic FGT electrode with non-magnetic graphene (Supplementary Section 9). These features suggest that the external magnetic field magnetizes the FGT electrode at 78 K and thus determines the spin orientations of charge carriers injected from the FGT/hBN ferromagnetic tunnelling contact. When negative V_b is applied to the heterostructure, those spin-down (spin-up) holes injected from FGT would selectively be confined in the valence band in the K (−K) valley (Fig. 3c,d), because of the spin–valley locking effect of a monolayer WSe_2[1–3]. The injected holes would then recombine with unpolarized electrons that tunnel from the graphene contact. Critically, due to the population imbalance and opposite optical selection rules between ±K valleys[1,3], the heterostructures yield the preferential EL emission of specific helicity.

Next, we operated the emitter in the positive bias region ($V_b > 0$ V) and explored the possibility of injecting spin-up (down) electrons from the FGT contact into the K (−K) valley of WSe_2. Figure 3f,g presents the helicity-resolved EL spectra, measured at $V_b = 2.4$ V, with the external magnetic field (0.5 T) pointing out of and into the sample plane, respectively. Notably, the results show the nearly equal EL intensity for either σ^+-polarized or σ^--polarized light detection, indicating that valley polarization is not initiated (Fig. 3e). These characteristics are distinct from the magneto-EL results derived in the negative bias region (Fig. 3a,b). We note that a similar phenomenon can be observed from other representative vdW heterostructures that we fabricated (Supplementary Section 10). This importantly indicates that injecting spin-polarized holes from FGT into WSe_2 can more effectively lead to valley polarization than injecting spin-polarized electrons from FGT.

What are the origins of larger valley polarization at negative V_b? One possibility is that WSe_2 possesses huge valence band spin–orbit splitting ($\Delta_v \approx 450$ meV), in contrast to the conduction band ($\Delta_c \approx 25$ meV)[1,2], and thus the processes of valley scattering of holes are severely suppressed. Indeed, the recent time-resolved Kerr rotation experiment reveals that the spin–valley lifetimes of holes in WSe_2 are extraordinary long (~2 μs), demonstrating the stable hole polarization, while the lifetimes of electrons are only ~130 ns (ref. [25]). The other possibility is that the spin injection efficiency of FGT varies with the polarity of V_b. To elucidate this, we performed first-principles calculations for a freestanding FGT monolayer and several vdW heterostructures based on density functional theory (Methods and Supplementary Section 11). Figure 4a shows the calculated band structure of the freestanding FGT monolayer. As can be seen, the spin-up and spin-down bands are shifted in energy because of the important exchange interaction in this two-dimensional magnet. The density of states in Fig. 4b also reflects the asymmetric behaviour in the majority-spin and minority-spin channels. Among the complicated spin-polarized bands in Fig. 4a, we focused on the two parabolic-like bands near the high-symmetry point K in the Brillouin zone around the Fermi level (E_f), forming two electron pockets at the Fermi surface. These two electron pockets (Fig. 4c) at K, with the opposite spin and an exchange splitting of about 0.15 eV between them, play important roles in valley polarization of WSe_2 (see Supplementary Section 11 for further discussion). In view of the spin polarization, one can identify two energy regions. The lower-energy region (light blue) has nearly 100% spin polarization (P) because of the only spin-down band therein. The higher-energy region (orange) contains both spin-up and spin-down parabolic bands and is thus of lower spin polarization, less than 40%. Figure 4e,f shows respectively the spin-decomposed partial density of states and spin polarization calculated using the k points along ΓK near K as indicated by the blue bar in Fig. 4d. Although the experimental E_f of the FGT in our sample is unknown due to the charge transfer from other layers in the heterostructure, it would be highly likely to locate within the orange region in Fig. 4c,f with low spin polarization. It has been reported that the possible E_f shift of the FGT heterostructure due to an applied electric field similar to ours is about ±0.1 eV (ref. [17]). Consequently, negative V_b would downshift E_f into the light-blue energy region with ~100% spin polarization (Fig. 4c,f), whereas E_f of FGT would remain in the orange energy region with low spin polarization under positive V_b, given that the V_b is applied onto the graphene contact.

To further confirm that the observed valley polarization is due to spin injection from the FGT contact, we measured the change of EL helicity while varying the out-of-plane magnetic field. As demonstrated in Fig. 5a, the EL helicity reverses sign around 0.1 T and its magnetic dependence exhibits a clear rectangular hysteresis loop with a saturation polarization of ~8%, a hallmark of ferromagnetic behaviour. To gain further insight, we employed polar RMCD microscopy to probe the out-of-plane magnetic order of the

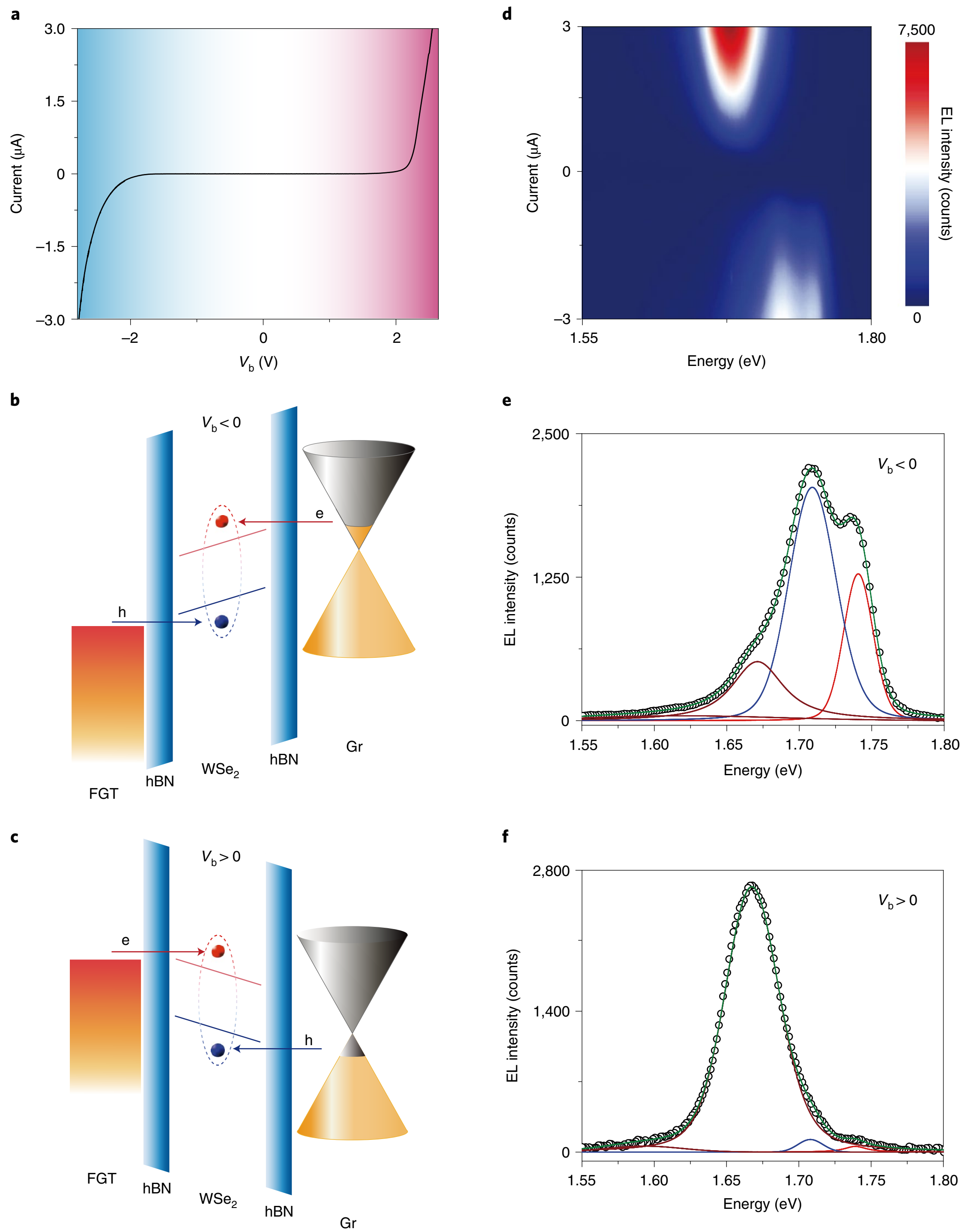

Fig. 2 | Electrical properties and EL of vdW heterostructures. a, *I*–*V* characteristics of the light-emitting heterostructures as V_b was applied across the graphene and FGT electrodes with the top FGT electrode grounded. The blue and pink shaded regions correspond to the negative and positive bias regions, respectively. **b**,**c**, Schematic of the electronic structure of vdW heterostructures, under negative V_b (**b**) and positive V_b (**c**). The applied bias voltage causes the electric potential drop between electrodes, which tilts the bands in hBN/WSe_2/hBN and shifts the Fermi energies of graphene and FGT, due to the quantum capacitance effect[34]. When the Fermi energies are close to the band edges of WSe_2, the electrons (e) and holes (h) will effectively tunnel from the two electrodes into WSe_2 and form excitons. The exciton recombination leads to EL generation. **d**, EL intensity map as a function of current injection. **e**,**f**, EL spectra measured at $V_b = -2.5$ V (**e**) and $V_b = 2.4$ V (**f**). Each EL spectrum was fitted by using Voigt functions to identify different excitonic peaks, where the red, blue and brown solid lines refer to the spectra of neutral (X^0), charged ($X^{+/-}$) and impurity-bound (X^{L1} and X^{L2}) excitonic emissions, respectively, and the green solid line is the cumulative fitting of all curves. The open black circles represent experimental data.

FGT top electrode (Methods) and observed a similar near-square hysteretic RMCD loop (Fig. 5b), a signature of the single magnetic domain and strongly anisotropic out-of-plane ferromagnetic ordering of FGT[14,15]. In addition, we found that the RMCD loop displays a coercive field of ~0.11 T, which is close to that found in the EL measurement.

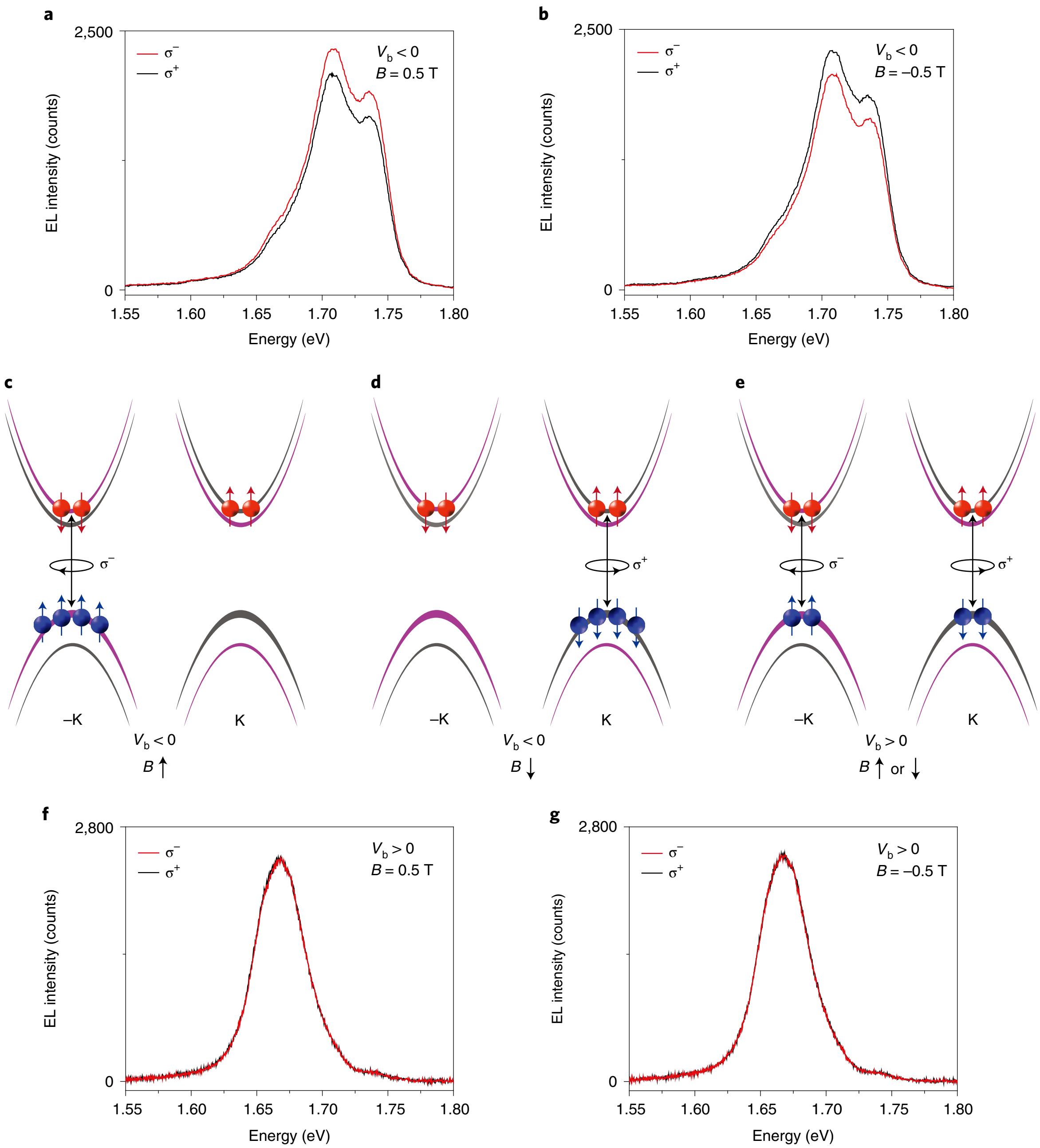

Fig. 3 | Electrical generation of valley polarization. a,**b**, Polarization-resolved EL spectra for σ^--polarized and σ^+-polarized detection. The magnetic field at 0.5 T pointed outwards (**a**) and inwards towards the surface of the heterostructure (**b**). The heterostructure was biased at −2.5 V. **c**,**d**, Schematic diagram showing the emissions of valley excitons while applying negative V_b to heterostructures. The FGT contact injects spin-up (**c**) and spin-down (**d**) holes (blue balls) into WSe_2, which would selectively be confined in the valence band in the −K and K valley, respectively, while the graphene contact injects unpolarized electrons (red balls) into WSe_2, which would be equally distributed in the two valleys. **e**, Schematic diagram showing the emissions of valley excitons while applying positive V_b to heterostructures. The electron–hole recombination in the −K and K valleys performs opposite EL helicity. In these schematic diagrams, the purple and grey curves denote the spin-down and spin-up, respectively, electron subbands of WSe_2. The spin–orbit splitting in the valence band (~450 meV) and conduction band (~25 meV) are sketched disproportionally for clarity. **f**,**g**, Polarization-resolved EL spectra for σ^--polarized and σ^+-polarized detection. The magnetic field at 0.5 T pointed outwards (**f**) and inwards towards the surface of the heterostructure (**g**). The heterostructure was biased at 2.4 V.

Finally, we verify that the measured magnetic-dependent EL helicity is not the result of magnetic circular dichroism of FGT (that is, differential transmission between σ^+-polarized and σ^--polarized light) or the Zeeman effect. To confirm this, we conducted a polarization-resolved magneto-PL experiment. Specifically, we illuminated the WSe_2 underneath the FGT/hBN ferromagnetic contact with linearly polarized light ($\lambda = 633$ nm). Under a magnetic field of 0.5 T, the σ^+ and σ^- polarizations of PL spectra exhibit the same peak energy and intensity (Fig. 5c). Furthermore, no hysteretic PL polarization was observed by sweeping the external magnetic field (Fig. 5d). These combined results provide clear evidence that the observed magnetic-dependent EL helicity stems from the injection of spin-polarized carriers.

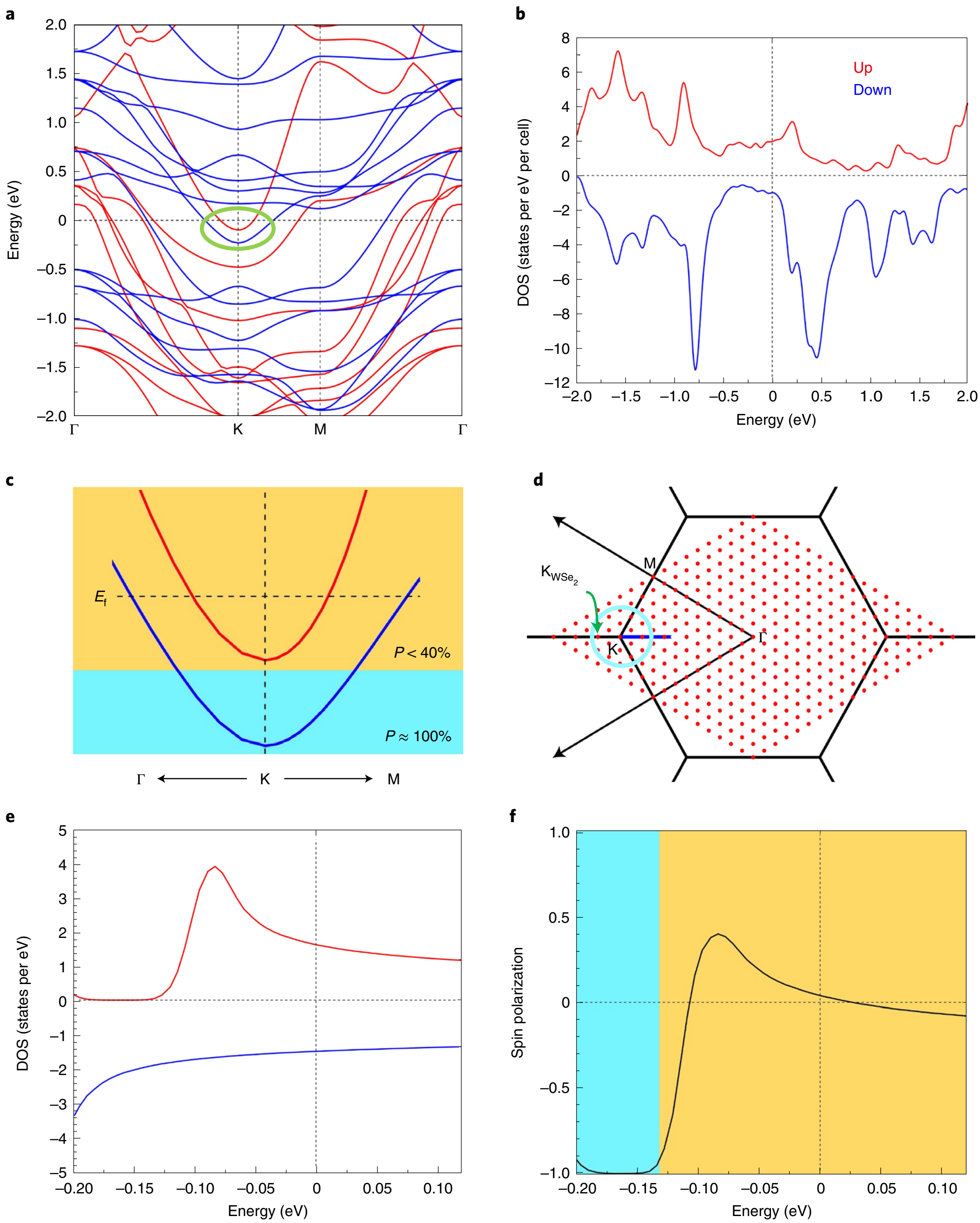

Fig. 4 | Electronic structures of freestanding FGT monolayer. **a**, Band structure of freestanding FGT monolayer. The red and blue curves represent the spin-up and spin-down bands, respectively. The green ellipse indicates two electron pockets at K. **b**, Density of states (DOS) of FGT monolayer. **c**, Magnified plot of the two electron pockets near the K point around the Fermi level as indicated by the green ellipse in **a**. The light-blue and orange colours indicate the fully spin-down (spin polarization $P \approx 100\%$) energy region and spin-up–spin-down mixed ($P < 40\%$) energy region, respectively. **d**, Hexagonal Brillouin zone of FGT monolayer. Black arrows are the basis vectors of the reciprocal space. Red dots are the Γ-centred equidistant *k*-point mesh used for self-consistent calculations. The light-blue circle indicates the electron pockets around K in **a** and **c**. The green arrow indicates the corresponding K point of the WSe_2 monolayer with the same orientation, which locates within the electron pocket (light-blue circle) of the FGT monolayer. The blue bar along Γ–K near K denotes the *k* points used for calculating the spin-decomposed partial density of states and spin polarization at the K valley in **e** and **f**, respectively. **e**. Spin-decomposed partial density of states calculated over the *k* points indicated by the blue bar in **d**. **f**, Spin polarization of the partial density of states in **e**. The orange region indicates the possible range of the Fermi level with low spin polarization. The light-blue region shows 100% spin polarization under negative V_b.

Conclusions

In summary, our work reveals the exciting possibilities of using a ferromagnetic FGT electrode to control the valley pseudospin degree of freedom of TMD. Importantly, our magneto-optoelectronic device structure is entirely composed of vdW materials. Thus, it can be readily integrated with diverse substrates or photonic structures

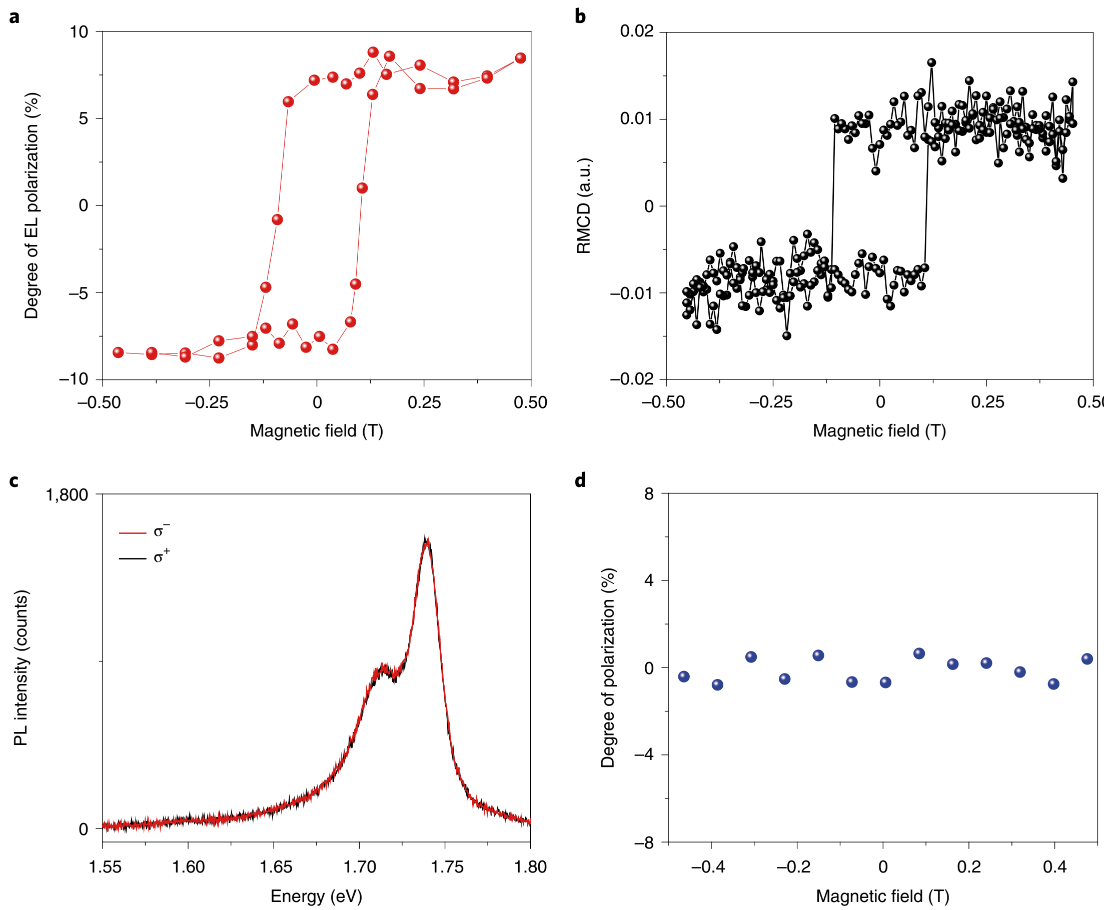

Fig. 5 | Magnetic field dependence of circular dichroism, EL and PL. a, The change of degree of EL polarization of neutral exciton emission over a cycle of the out-of-plane magnetic field. The result exhibits a hysteresis loop. **b**, Polar RMCD signal for the FGT flake used in vdW heterostructures. **c**, Polarization-resolved PL spectra for σ^--polarized and σ^+-polarized detection. The incident laser is linearly polarized and the magnetic field is 0.5 T, pointing outwards towards the surface of the heterostructures. **d**, Magnetic field dependence of PL helicity, obtained using linearly polarized laser excitation.

without lattice-matching constraint, greatly enhancing their applicability[26,27]. On the basis of our framework, we anticipate that electrical control of valley polarization near room temperature could potentially be achieved, considering the recent rapid expansion of the vdW materials library. For instance, the top FGT electrode can be replaced with emerging materials, such as Fe_5GeTe_2 and $MnSe_x$, which are metals with ferromagnetism near room temperature[28,29]. Additionally, the recently developed chalcogenide-alloyed TMD monolayers can be exploited, as they possess strong spin–valley characteristics at room temperature, confirmed by the helicity-dependent PL measurements[30]. Beyond this, it is also noteworthy that many of the above materials can be synthesized at wafer scale[31–33]. Such advancement offers tremendous opportunities to realize scalable valleytronics for practical information processing and computing applications.

Online content

Any methods, additional references, Nature Research reporting summaries, source data, extended data, supplementary information, acknowledgements, peer review information; details of author contributions and competing interests; and statements of data and code availability are available at https://doi.org/10.1038/s41565-022-01115-2.

Received: 28 October 2021; Accepted: 7 March 2022;
Published online: 2 May 2022

References

1. Xu, X. D., Yao, W., Xiao, D. & Heinz, T. F. Spin and pseudospins in layered transition metal dichalcogenides. *Nat. Phys.* **10**, 343–350 (2014).
2. Xiao, D., Liu, G. B., Feng, W. X., Xu, X. D. & Yao, W. Coupled spin and valley physics in monolayers of MoS_2 and other group-VI dichalcogenides. *Phys. Rev. Lett.* **108**, 196802 (2012).
3. Mak, K. F., Xiao, D. & Shan, J. Light–valley interactions in 2D semiconductors. *Nat. Photon.* **12**, 451–460 (2018).
4. Zeng, H. L., Dai, J. F., Yao, W., Xiao, D. & Cui, X. D. Valley polarization in MoS_2 monolayers by optical pumping. *Nat. Nanotechnol.* **7**, 490–493 (2012).
5. Mak, K. F., He, K. L., Shan, J. & Heinz, T. F. Control of valley polarization in monolayer MoS_2 by optical helicity. *Nat. Nanotechnol.* **7**, 494–498 (2012).
6. Cao, T. et al. Valley-selective circular dichroism of monolayer molybdenum disulphide. *Nat. Commun.* **3**, 887 (2012).
7. Mak, K. F., McGill, K. L., Park, J. & McEuen, P. L. The valley Hall effect in MoS_2 transistors. *Science* **344**, 1489–1492 (2014).
8. Onga, M., Zhang, Y. J., Ideue, T. & Iwasa, Y. Exciton Hall effect in monolayer MoS_2. *Nat. Mater.* **16**, 1193–1197 (2017).
9. Ye, Y. et al. Electrical generation and control of the valley carriers in a monolayer transition metal dichalcogenide. *Nat. Nanotechnol.* **11**, 598–602 (2016).
10. Sanchez, O. L., Ovchinnikov, D., Misra, S., Allain, A. & Kis, A. Valley polarization by spin injection in a light-emitting van der Waals heterojunction. *Nano Lett.* **16**, 5792–5797 (2016).
11. Gong, C. & Zhang, X. Two-dimensional magnetic crystals and emergent heterostructure devices. *Science* **363**, eaav4450 (2019).
12. Gibertini, M., Koperski, M., Morpurgo, A. F. & Novoselov, K. S. Magnetic 2D materials and heterostructures. *Nat. Nanotechnol.* **14**, 408–419 (2019).
13. Burch, K. S., Mandrus, D. & Park, J. G. Magnetism in two-dimensional van der Waals materials. *Nature* **563**, 47–52 (2018).

14. Fei, Z. Y. et al. Two-dimensional itinerant ferromagnetism in atomically thin Fe_3GeTe_2. *Nat. Mater.* **17**, 778–782 (2018).
15. Tan, C. et al. Hard magnetic properties in nanoflake van der Waals Fe_3GeTe_2. *Nat. Commun.* **9**, 1554 (2018).
16. Deng, Y. J. et al. Gate-tunable room-temperature ferromagnetism in two-dimensional Fe_3GeTe_2. *Nature* **563**, 94–99 (2018).
17. Wang, Z. et al. Tunneling spin valves based on Fe_3GeTe_2/hBN/ Fe_3GeTe_2 van der Waals heterostructures. *Nano Lett.* **18**, 4303–4308 (2018).
18. Schaibley, J. R. et al. Valleytronics in 2D materials. *Nat. Rev. Mater.* **1**, 16055 (2016).
19. Withers, F. et al. Light-emitting diodes by band-structure engineering in van der Waals heterostructures. *Nat. Mater.* **14**, 301–306 (2015).
20. Liu, C. H. et al. Nanocavity integrated van der Waals heterostructure light-emitting tunneling diode. *Nano Lett.* **17**, 200–205 (2017).
21. Withers, F. et al. WSe_2 light-emitting tunneling transistors with enhanced brightness at room temperature. *Nano Lett.* **15**, 8223–8228 (2015).
22. Jones, A. M. et al. Optical generation of excitonic valley coherence in monolayer WSe_2. *Nat. Nanotechnol.* **8**, 634–638 (2013).
23. Huang, J. N., Hoang, T. B. & Mikkelsen, M. H. Probing the origin of excitonic states in monolayer WSe_2. *Sci. Rep.* **6**, 22414 (2016).
24. Wang, G. et al. Valley dynamics probed through charged and neutral exciton emission in monolayer WSe_2. *Phys. Rev. B* **90**, 075413 (2014).
25. Dey, P. et al. Gate-controlled spin–valley locking of resident carriers in WSe_2 monolayers. *Phys. Rev. Lett.* **119**, 137401 (2017).
26. Liu, C. H., Zheng, J. J., Chen, Y. Y., Fryett, T. & Majumdar, A. Van der Waals materials integrated nanophotonic devices. *Opt. Mater. Express* **9**, 384–399 (2019).
27. Brar, V. W., Sherrott, M. C. & Jariwala, D. Emerging photonic architectures in two-dimensional opto-electronics. *Chem. Soc. Rev.* **47**, 6824–6844 (2018).
28. May, A. F. et al. Ferromagnetism near room temperature in the cleavable van der Waals crystal Fe_5GeTe_2. *ACS Nano* **13**, 4436–4442 (2019).
29. O'Hara, D. J. et al. Room temperature intrinsic ferromagnetism in epitaxial manganese selenide films in the monolayer limit. *Nano Lett.* **18**, 3125–3131 (2018).
30. Liu, S. et al. Room-temperature valley polarization in atomically thin semiconductors via chalcogenide alloying. *ACS Nano* **14**, 9873–9883 (2020).
31. Huang, P. et al. Recent advances in two-dimensional ferromagnetism: materials synthesis, physical properties and device applications. *Nanoscale* **12**, 2309–2327 (2020).
32. Roemer, R., Liu, C. & Zou, K. Robust ferromagnetism in wafer-scale monolayer and multilayer Fe_3GeTe_2. *npj 2D Mater. Appl.* **4**, 33 (2020).
33. Kang, K. et al. High-mobility three-atom-thick semiconducting films with wafer-scale homogeneity. *Nature* **520**, 656–660 (2015).
34. Yu, G. L. et al. Interaction phenomena in graphene seen through quantum capacitance. *Proc. Natl Acad. Sci. USA* **110**, 3282–3286 (2013).

Methods

Fabrication of vdW heterostructures. The graphene, hBN and FGT flakes were mechanically exfoliated. WSe_2 monolayers were prepared using a CVD method due to the ease of obtaining large and uniform flakes. The other reason for using CVD-grown WSe_2 flakes is because they generally exhibit higher PL helicity than our exfoliated WSe_2 (only ~10 to 15%). This might be because CVD WSe_2 contains a higher defect density, limiting the valley depolarization processes[35].

To create the vdW heterostructures, we exploited the dry transfer technique[36] to stack the selected vdW flakes in the vertical direction. The assembled FGT/hBN/WSe_2/hBN/graphene heterostructures (from top to bottom) were then transferred onto a Si/SiO_2 substrate with two separate prepatterned palladium (40 nm) metal electrodes. During the transfer process, the bottom graphene and top FGT layers were aligned to contact the separate metal electrodes. All the above transfer and material exfoliation steps were conducted in a nitrogen-filled glove box, where the oxygen and water concentration are below 0.5 ppm, to minimize oxidation of materials. The transferred vdW heterostructures were then taken out of the glove box and wire bonded onto a chip carrier. After wire bonding, they were immediately loaded into the cryogenic system.

Optoelectronic measurements. The fabricated vdW heterostructures were wire bonded to chip carriers and mounted on the cold finger of a continuous-flow cryostat (Janis ST 500) with an electromagnet to conduct different optoelectronic measurements at 78 K. When conducting the EL and PL experiments, the generated luminescence signals from vdW heterostructures were captured by an aspheric lens (numerical aperture, 0.55) and then analysed by a grating spectrometer (Andor Shamrock 500i) equipped with an Andor Newton 920 CCD camera. For PL experiments, the samples were excited with a 1.96 eV laser focused to a 1 µm spot size.

When conducting the RMCD experiments, a power-stabilized and linearly polarized light ($\lambda = 633$ nm) was sinusoidally modulated between right and left circular polarization at 50.1 kHz by a photoelastic modulator. The modulated light was focused onto vdW heterostructures at normal incidence using an aspheric lens. The light reflected from the heterostructures was then passed through the same lens and detected by a balanced amplified photodetector to measure the difference in reflectivity between right and left circularly polarized light as detailed in refs. [37,38].

First-principles calculations. First-principles calculations were performed using the Vienna Ab initio Simulation Package (VASP)[39–41] with the Perdew–Burke–Ernzerhof exchange–correlation functional[42] used in the generalized gradient approximation based on density functional theory. The cutoff energy of 500 eV was adopted for the plane-wave basis. A Γ-centred $18 \times 18 \times 1$ k mesh for monolayer FGT and a Γ-centred $18 \times 18 \times 4$ k mesh for bulk FGT were used in geometry optimization and self-consistent field calculations. A vacuum layer with thickness of ~15 Å was used to avoid interlayer interactions between periodically repeated slabs. We have considered several kinds of monolayer and vdW heterostructure in this work. The freestanding case, which gives a simple and clear demonstration of the source of the spin-polarization current, is presented in the manuscript. The other cases are shown in Supplementary Section 11. For all cases, the geometry of the whole system was optimized with the residual forces below 0.01 eV Å^{-1}.

Data availability

All other data that support the plots within this paper and other findings of this study are available from the corresponding authors upon reasonable request. Source data are provided with this paper.

References

35. McCreary, K. M., Currie, M., Hanbicki, A. T., Chuang, H. J. & Jonker, B. T. Understanding variations in circularly polarized photoluminescence in monolayer transition metal dichalcogenides. *ACS Nano* **11**, 7988–7994 (2017).
36. Liu, Y. et al. Van der Waals heterostructures and devices. *Nat. Rev. Mater.* **1**, 16042 (2016).
37. Katsuaki, S. Measurement of magneto-optical Kerr effect using piezo-birefringent modulator. *Jpn J. Appl. Phys.* **20**, 2403 (1981).
38. Wang, Z. et al. Electric-field control of magnetism in a few-layered van der Waals ferromagnetic semiconductor. *Nat. Nanotechnol.* **13**, 554–559 (2018).
39. Kresse, G. & Hafner, J. Ab-initio molecular-dynamics simulation of the liquid-metal amorphous–semiconductor transition in germanium. *Phys. Rev. B* **49**, 14251–14269 (1994).
40. Kresse, G. & Furthmuller, J. Efficient iterative schemes for ab initio total-energy calculations using a plane-wave basis set. *Phys. Rev. B* **54**, 11169–11186 (1996).
41. Blöchl, P. E. Projector augmented-wave method. *Phys. Rev. B* **50**, 17953–17979 (1994).
42. Perdew, J. P., Burke, K. & Ernzerhof, M. Generalized gradient approximation made simple. *Phys. Rev. Lett.* **77**, 3865–3868 (1996).

Acknowledgements

We thank K. L. Seyler for useful discussions and C.-B. Huang for sharing electronic instruments. C.-H.L. acknowledges support from the National Tsing Hua University (110QI039E1) and the Ministry of Science and Technology of Taiwan (107-2112-M-007-002-MY3, 109-2112-M-007-032-MY3). H.-T.J. acknowledges support from the Ministry of Science and Technology of Taiwan (109-2112-M-007-034-MY3). H.-T.J. also thanks NCHC, CINCNTU, AS-iMATE-109-13 and CQT-NTHU-MOE, Taiwan, for support.

Author contributions

C.-H.L. and H.-T.J. supervised the project. Y.-C.Y. synthesized CVD WSe_2, assisted by P.-W.C. J.-X.L. and W.-Q.L. fabricated the vdW heterostructures, assisted by P.-L.C. C.-H.L. conceived the experiments. J.-X.L. and W.-Q.L. performed the measurements, assisted by T.-Y.C. and C.-H.L. S.-H.H. and H.-T.J. provided theoretical support. All authors contributed to the discussion of the data in the paper and Supplementary Information.

Competing interests

The authors declare no competing interests.

Additional information

Supplementary information The online version contains supplementary material available at https://doi.org/10.1038/s41565-022-01115-2.

Correspondence and requests for materials should be addressed to Horng-Tay Jeng or Chang-Hua Liu.

Peer review information *Nature Nanotechnology* thanks Zheng Han and the other, anonymous, reviewer(s) for their contribution to the peer review of this work.